



Contents lists available at ScienceDirect

# Medical Image Analysis

journal homepage: [www.elsevier.com/locate/media](http://www.elsevier.com/locate/media)

## Gaze-Contingent Motor Channelling, haptic constraints and associated cognitive demand for robotic MIS

George P. Mylonas<sup>a,\*</sup>, Ka-Wai Kwok<sup>a</sup>, David R.C. James<sup>b</sup>, Daniel Leff<sup>b</sup>, Felipe Orihuela-Espina<sup>a</sup>, Ara Darzi<sup>b</sup>, Guang-Zhong Yang<sup>a</sup>

<sup>a</sup> Royal Society/Wolfson Foundation Medical Image Computing Laboratory, Imperial College London, London SW7 2AZ, United Kingdom

<sup>b</sup> Department of Biosurgery and Surgical Technology, Queen Elizabeth the Queen Mother Wing (QEOM), St. Mary's Campus, Imperial College London, London W2 1NY, United Kingdom

### ARTICLE INFO

#### Article history:

Received 13 September 2009

Received in revised form 5 July 2010

Accepted 22 July 2010

Available online 1 August 2010

#### Keywords:

Robotic surgery

Minimally invasive surgery

Eye tracking

Gaze-contingent control

Virtual fixtures

### ABSTRACT

The success of MIS is coupled with an increasing demand on surgeons' manual dexterity and visuomotor coordination due to the complexity of instrument manipulations. The use of master–slave surgical robots has avoided many of the drawbacks of MIS, but at the same time, has increased the physical separation between the surgeon and the patient. Tissue deformation combined with restricted workspace and visibility of an already cluttered environment can raise critical issues related to surgical precision and safety. Reconnecting the essential visuomotor sensory feedback is important for the safe practice of robot-assisted MIS procedures. This paper introduces a novel gaze-contingent framework for real-time haptic feedback and virtual fixtures by transforming visual sensory information into physical constraints that can interact with the motor sensory channel. We demonstrate how motor tracking of deforming tissue can be made more effective and accurate through the concept of *Gaze-Contingent Motor Channelling*. The method is also extended to 3D by introducing the concept of *Gaze-Contingent Haptic Constraints* where eye gaze is used to dynamically prescribe and update safety boundaries during robot-assisted MIS without prior knowledge of the soft-tissue morphology. Initial validation results on both simulated and robot assisted phantom procedures demonstrate the potential clinical value of the technique. In order to assess the associated cognitive demand of the proposed concepts, functional Near-Infrared Spectroscopy is used and preliminary results are discussed.

© 2010 Elsevier B.V. All rights reserved.

### 1. Introduction

Despite major advances in current robotic systems, the somato-sensory loop is heavily impacted by the use of remote manipulators. Most motor and sensory channels are interrupted. The flow of information is limited to the use of the hands and the fingers, with the only stimulus available being the visual. For the visual channel, due to the use of stereoscopic optics, current systems are able to maintain high fidelity and bandwidth on the flow of visual information, although some attenuation is also expected. With systems like the da Vinci (Intuitive Surgical, Sunnyvale, CA), motion scaling in proportion to the visual magnification and the alignment of the visual and motor axes, has also promoted propri-

\* Corresponding author. Address: Institute of Biomedical Engineering, 509 Bessemer, South Kensington Campus, Imperial College, London SW7 2AZ, United Kingdom. Tel.: +44 20 7594 0769; fax: +44 20 7581 8024.

E-mail addresses: [george.mylonas@imperial.ac.uk](mailto:george.mylonas@imperial.ac.uk) (G.P. Mylonas), [kkwok07@imperial.ac.uk](mailto:kkwok07@imperial.ac.uk) (K.-W. Kwok), [d.james@imperial.ac.uk](mailto:d.james@imperial.ac.uk) (D.R.C. James), [d.leff@imperial.ac.uk](mailto:d.leff@imperial.ac.uk) (D. Leff), [f.orihuela-espina@imperial.ac.uk](mailto:f.orihuela-espina@imperial.ac.uk) (F. Orihuela-Espina), [a.darzi@imperial.ac.uk](mailto:a.darzi@imperial.ac.uk) (A. Darzi), [g.z.yang@imperial.ac.uk](mailto:g.z.yang@imperial.ac.uk) (G.-Z. Yang).

ception to a certain extent. In the current systems, haptic information is limited, which is expected to have a direct impact on the Perception–Cognition–Action capabilities of the operator, as well as hand–eye coordination. Furthermore, the lack of haptic feedback can also impose a potential safety risk.

Work published by Rosenberg and others (Rosenberg, 1993; Park et al., 2001) introduced the concept of *Virtual Fixtures* (VFs) for enhancing the performance and safety of MIS by enhancing the operator's motor ability. In general virtual fixtures can be divided into two categories: *guidance virtual fixtures* (GVFs) and *forbidden-region virtual fixtures* (FRVFs). With robotic systems incorporating 3D vision, virtual fixtures can help the surgeon to locate particular tissue structures or to dissect near a structure while enforcing a safety margin to prevent injury to the structure itself. In terms of using FRVFs to enhance surgical safety, *active constraints* (ACs) were first introduced by Davies (Davies, 2006; Davies et al., 2006). They represent an interaction mode where the motion or forces exerted by the robot is a subset or limited version of those requested by the operator. In this way, the robot is prevented from moving outside a safe region, ensuring the preservation of critical features.

There are several important considerations for the practical application of virtual fixtures in robot-assisted MIS. The first is user defined selection of the appropriate *VF* geometry. Currently, this is assisted and performed through computer vision recognition, modeling of tissue deformation and registration of pre-operatively acquired 3D patient specific data (Li and Taylor, 2004; Abbott et al., 2007; Ren et al., 2008). Second, *VF* assistance should be tuned based on the task at hand and the surgeon's actions within that context. Research groups are exploring methods for automatic tuning of virtual fixture strength based for example on Hidden Markov model recognition of operator motions (Okamura, 2004). Finally, there is significant uncertainty in robot position relative to the anatomical structures onto which it is required to place accurate virtual fixtures. All the above requirements and their intrinsic uncertainty and instability when it comes to in situ, in vivo implementation, demonstrate the current difficulties in effectively utilizing virtual fixtures.

The ability to utilise the information acquired through the eyes and in guiding the hands to complete a given task is commonly referred to as *hand–eye coordination*. There is an intricate relationship between the hands and the eyes and extensive research has been focussed on understanding of the underlying mechanisms governing this relationship. Hand–eye coordination is not an innate ability; it is slowly learnt and refined from birth. Based on the example of how certain individuals – like athletes – excel in hand–eye coordination, it is obvious that it can also be fine-tuned and adapted to certain skills through practice and experience. There are numerous studies demonstrating skills improvement through practice and experience. In the MIS domain, particularly in hand–eye coordination and skills assessment studies, Leong et al. (2008) and Leong (2009) have shown that as the subject's skill levels improve through adaptation to a new sensorimotor transformation, their movements between two targets become more consistent. Evaluating the spatiotemporal relationship between the hands and the eyes (fixation point), it was found that the eyes tend to search ahead of the hand. In a laparoscopic dissection task, it was shown that the instrument only precedes the eye movements in early skills acquisition of a complex procedure.

In terms of learning a novel visuomotor task for which the subjects had to control a cursor on a screen and hit a target, Sailer et al. found three stages of learning, as defined by performance of the task and also the gaze–cursor relationship (Sailer et al., 2005). During the early exploratory phase, gaze tends to follow the cursor, with occasional glances to the target. The saccades sizes, in this case, are generally small (3–4°). During the skill acquisition phase, this is changed to a predictive behaviour, with fixations leading the cursor by up to 300 ms. It was found that saccades sizes were larger (4–12°), and more were directed towards the target. Finally, at the skill refinement stage, gaze went directly to the next target, with either a single saccade, or a large and one small saccade. These are important findings that underpin some of the concepts used in this paper.

The domain of *VFs* seems to provide fertile grounds where the visual and motor channels naturally meet and breed task improvement. However, the role of human vision still remains “observatory” by not directly affecting the external world. Also, most of the existing *VF* techniques require explicit knowledge of the soft-tissue morphology by means of pre-operative data acquisition and subsequent planning. This means accurate intra-operative registration is important, which is known to be difficult for soft tissue with large intra-operative deformation. The proposed concept of *Gaze-Contingent Motor Channelling*, allows the visual modality to directly interact with the external world by using the user's hand as a proxy. As it will be shown in the following sections, this synergy can improve motor ability and also overcome certain limitations associated with the use of *VFs* intra-operatively.

The details of *GC motor channelling* will be discussed in the following sections. As an introduction to the nature and the novelty of the proposed framework, Fig. 1 further illustrates a high level schematic representation of the proposed visuomotor transformations involved in visually guided motor tasks. The way that this is different to the natural process lies in the introduction of an additional pathway, shown by the counter-clockwise arrows. This pathway allows flow and direct transformation of raw visual information into motor coordinates. In a sense, we interfere with the sensorimotor map of the brain and study the consequences of removing, to certain extent, the brain as a “middleman” by allowing direct mapping of visual to motor coordinates. The potential impact of the technique on cognitive process is discussed at the very end of the paper.

The purpose of this paper is to introduce a novel gaze-contingent scheme for realizing real-time haptic constraints in situ. The concept transubstantiates visual sensory information into physical entities that can interact with the motor sensory channel. We demonstrate how motor tracking of deforming tissue can be made more effective, accurate and safer through the use of *Gaze-Contingent Motor Channelling (GC motor channelling)* and *Gaze-Contingent Haptic Constraints (GC haptic constraints)*. One important part of the proposed framework is the use of 3D eye gaze to dynamically prescribe and update safety boundaries during robot-assisted MIS without prior knowledge of the soft-tissue morphology. The work presented here further extends our existing experience in real-time eye tracking (Yang et al., 2002; Mylonas et al., 2004, 2005, 2006; Noonan et al., 2008; Kwok et al., 2009). To our knowledge, this is the first study that successfully bridges the visual and motor modalities by shifting the computational burden towards perceptually enabled channels in the realm of the Perceptual Docking paradigm introduced by Yang et al. (2008). In the last part of the paper, we examine the potential cognitive demand that this approach imposes onto the user through the use of functional Near-Infrared Spectroscopy (*fNIRS*). Initial validation results on both simulated and robot assisted 2D and 3D phantom experiments demonstrate the potential clinical value of the technique. Furthermore, brain activation patterns are studied to expose the underlying processes involved and how the proposed concepts affect mental processing.

## 2. Materials and methods

In the sections to follow, the proposed concept of *Gaze-Contingent Motor Channelling* is first demonstrated in a 2D synthetic environment and subsequently extended to manipulations in 3D synthetic scenes. In each case, different aspects of the synergy between the human visual and motor channels are demonstrated. For allowing interactions between the two channels, eye tracking and haptic manipulation devices are used. The effectiveness of the proposed concept is demonstrated on a synthetically generated beating heart.

### 2.1. GCMC methods

For 2D haptic interactions, a synthetic surgical scene with a deforming soft-tissue surface is used. During simulation, a virtual endoscope camera observes a deformable mesh, which is texture-mapped using footage from an in vivo robot assisted totally endoscopic coronary artery bypass grafting procedure. The mesh is repeatedly deformed by a function combining respiratory and cardiac induced tissue deformation of varying frequencies (Fig. 2 top). For simplicity, we chose the respiratory component to be a rigid translation and the cardiac component to be represented by a mixture of Gaussians with respect to a selected deformation

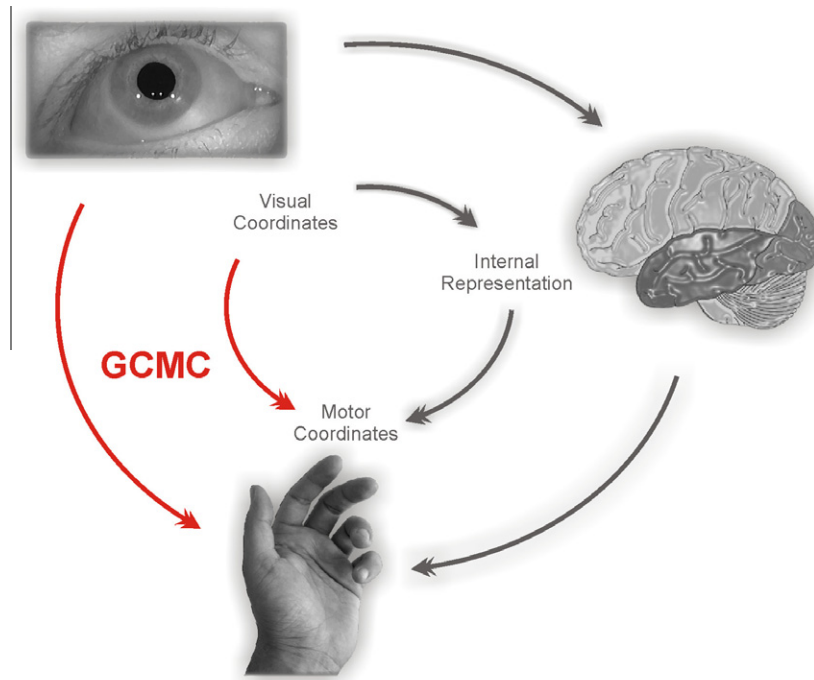


**Fig. 1.** High level schematic of the visuomotor transformations involved in a visually guided motor task. In the clockwise arrows direction, target coordinates on the visual frame are transformed into coordinates on the motor frame through the brain's internal mechanisms. In the introduced *GC motor channelling* paradigm, an additional pathway (counter-clockwise arrows) is established that allows flow and direct transformation of raw visual information into motor coordinates.

centre. The two deformations are combined with linear weighting. The equation for the deformation applied to a vertex at time  $T$  is:

$$\mathbf{V}_{t+1} = \mathbf{V}_0 + \sin(\phi) \begin{bmatrix} W_x^s e^{-W_x^d (V_x - C_x)} \\ W_y^s e^{-W_y^d (V_y - C_y)} \\ W_z^s e^{-W_z^d (V_z - C_z)} \end{bmatrix} + \sin(\varphi) \begin{bmatrix} W_x^r T_x \\ W_y^r T_y \\ W_z^r T_z \end{bmatrix} \quad (1)$$

The first sinusoidal product represents the cardiac deformation and the second product a rigid breathing translation. The breathing translation is rigid because of the difference in scale of the two motions. In (1), the terms  $W^s$  and  $W^r$  represent the weight of the cardiac and respiratory motion components respectively and  $W^d$  the damping weight.  $\mathbf{V}_0$  represents the original vertex of the surface,  $C$  is the centre of deformation and  $V$  is the vertex coordinates. The sinusoidal terms specify the frequencies of oscillation  $\varphi$  and  $\phi$  in such a way that a full sinusoidal cycle is completed in  $N$  steps. This means that for instance a frequency of 25 will generate 25 frames for a complete sinusoidal cycle. Finally, the 3D mesh is projected to 2D and a video sequence of the artificially deformed tissue is generated from the extracted image series and displayed on a monitor for the subsequent 2D experiments (Fig. 2).

Eye tracking for the 2D experiments was performed using a Tobii  $\times 50$  (Tobii Technologies AB, Sweden) stand-alone eye tracker. This is an infrared video-based remote eye-tracking system used to record fixation points on a screen at 50 Hz with an accuracy of  $0.5^\circ$  and drift  $<1$  degree across the work plane. The system allows for a certain amount of head movement within a working volume with dimensions of  $30 \times 16 \times 20 \text{ cm}^3$  (Tobii-Technology, 2003). Prior to eye tracking, subject specific calibration is necessary and the gaze data is median filtered with a window size of 140 ms.

To allow for real-time tissue interaction, a haptic device was used to control a virtual surgical tool (proxy) within the FOV (Fig. 3). For these experiments, a Phantom Premium 1.5/6DOF haptic device from SensAble Technologies (MA) was used. The device provides a workspace with translational dimensions  $381 \times 267 \times 191 \text{ mm}^3$  ( $W \times H \times D$ ) and rotational dimensions

( $297^\circ, 260^\circ, 335^\circ$ ) (Yaw, Pitch, Roll). The nominal position resolution in terms of translation is 860 dpi/0.03 mm and in terms of rotation  $0.0023^\circ$  (yaw and pitch) and  $0.0080^\circ$  (roll). The backdrive friction in the three axes is 0.04 N. The maximum exertable force and torque at nominal position (orthogonal arms) is 8.5 N for translation and 515 m Nm (yaw and pitch) and 170 m Nm (roll). The respective continuous force and torque are 1.4 N for translation, 188 n Nm (yaw and pitch) and 48 m Nm (roll). Also, the stiffness is 3.5 N/mm and the apparent inertia at the tip is 136 g. The device is able to provide force feedback and position sensing in 6DOF, namely on the  $x, y, z$  axes and the  $T_x, T_y, T_z$  rotations and is interfaced to a PC through the parallel port.

The *GC motor channelling* interaction with the simulated 2D surgical scene is applied based on the relative separation between the user's fixation point on the screen and the 2D position of the manipulated surgical instrument (both on the screen frame-of-reference  $\mathbf{S}$  as shown in Fig. 3). The direction of the exerted force is towards the fixation point. Hand-motion scaling as well as different force profiles can be introduced in order to assess the optimal manipulation profile to be used in practical applications. Fig. 3 illustrates the actual setup used for this experiment. For the 2D case described here, the coordinates are projected to the screen frame-of-reference.

## 2.2. Experimental setup for GC motor channelling

To assess the effectiveness of the proposed *GC motor channelling* framework in a 2D motor tracking task, a moving target is introduced to the synthetically generated deforming 2D tissue. The target accurately follows the tissue deformation and during a full cycle it spans an area corresponding to  $8.5^\circ$  of horizontal and  $5.5^\circ$  of vertical visual angle. The coordinates of the target are registered and known on a per video-frame basis (Fig. 2). The composite frequency of oscillation of the target is constant at 0.205 Hz.

For this study, seven subjects were recruited and presented with the video of the deforming tissue. All subjects have engineering

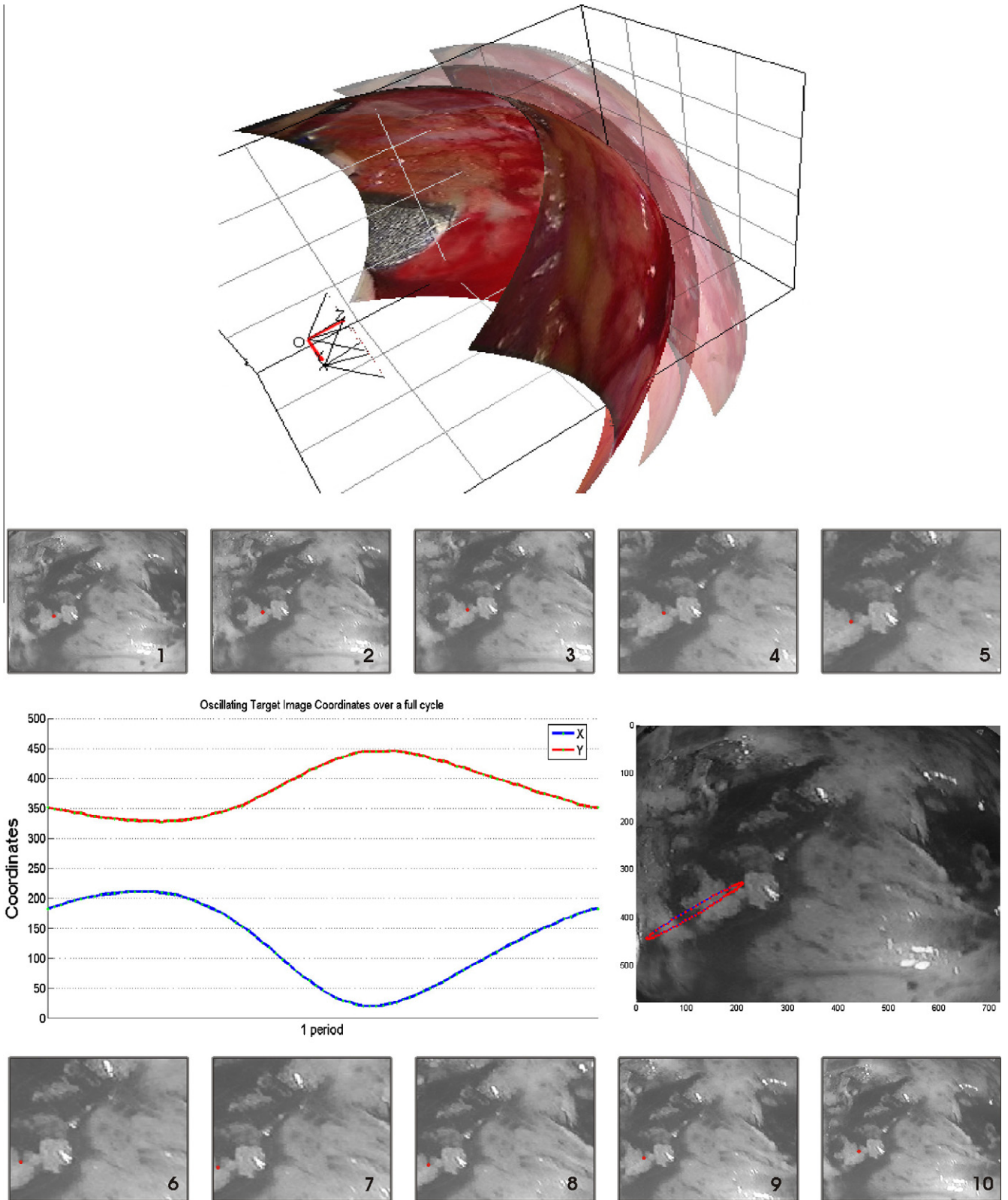


**Fig. 2.** The figure on the top shows the synthetic surgical scene generator used to generate the artificially deforming tissue sequences used in the GCMC study. The graph shows the X and Y coordinates of the deforming target trajectory over one period. The images are snapshots at equidistant points in time showing the appearance of the deforming tissue and the position of the target over this period.

background, six males and one female, aged between 22 and 38 years old, all right handed and completely inexperienced with the concept. The subjects were given as much time as they needed to familiarize themselves with the Phantom manipulator and the

basic concept of *GC motor channelling*. Their task was to track the moving target as accurately as possible with the tip of the virtual instrument. During the experiment, eight different manipulation profiles of the haptic device were introduced in the order as they

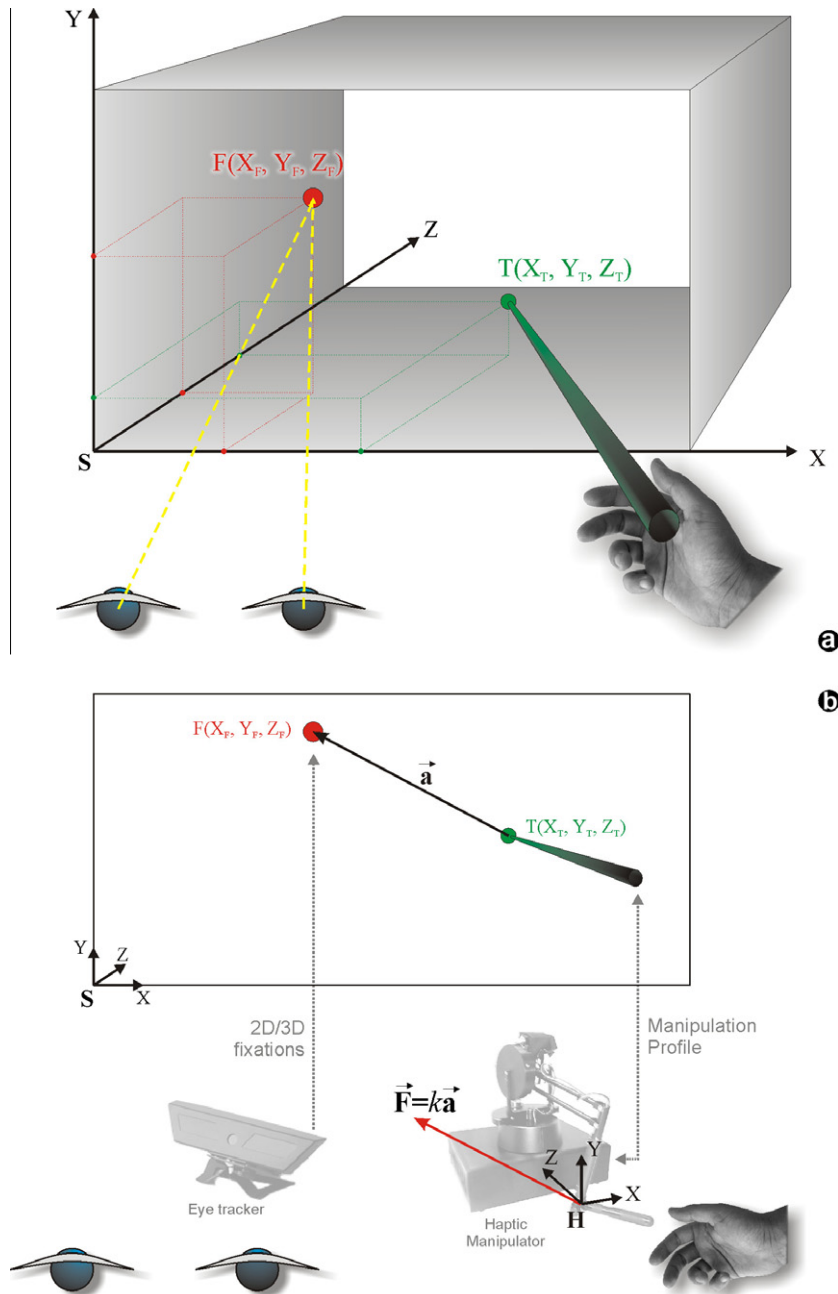


**Fig. 3.** Schematic illustration of the *GC motor channelling* study concept (a) and the proposed *GC motor channelling* framework (b). The setup involves the use of an eye tracker to localize the 2D/3D fixation  $F$  of the user on a screen or stereoscope. Manipulation of a virtual tool  $T$  is achieved through a haptic manipulator. Depending on the Cartesian distance between  $F$  and  $T$ , a force  $\vec{F}$  toward the fixation point is exerted on the hand of the user via the haptic manipulator as  $\vec{F} = k\vec{a}$ .

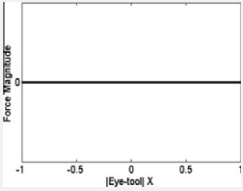
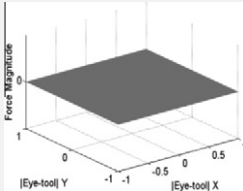
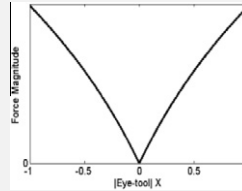
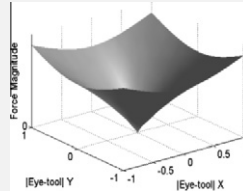
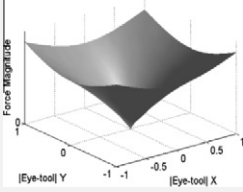
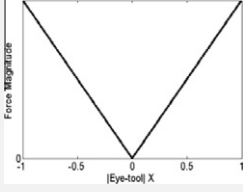
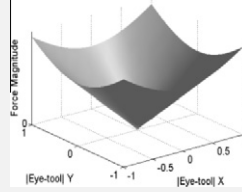
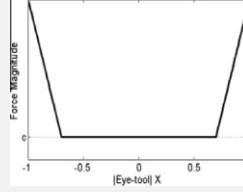
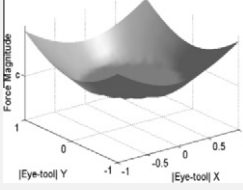
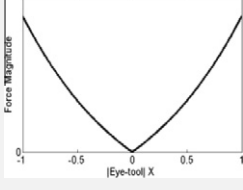
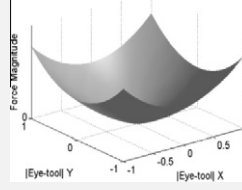
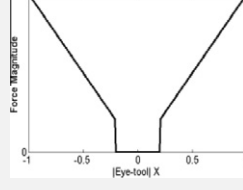








appear in Table 1. High values of hand-motion scaling mean small hand movements being translated into large displacements of the virtual tool in the world coordinates. For high motion scaling, a factor of 3 was used. This means that the hand motion is amplified three times by the time it is executed by the virtual tool. In a real scenario, this would correspond to an MIS surgical tool being pivoted at a distance of 3/4 its total length from the distal point. A unit scaling factor provides a 1:1 mapping between the hand and the tool. This transformation involves two steps. First, the haptic coordinate system, which coincides with the world coordinate system ( $H$  in Fig. 3), is mapped to the screen coordinate system, i.e., pixels ( $S$  in Fig. 3). A final transformation is performed to map the screen coordinates back to the world coordinates. This last step is to take into consideration the screen size and resolution in order to

correctly match the amplitude of the hand movement with the resulting apparent movement of the virtual tool. For tasks using manipulation profiles 1 and 2, no force is exerted on the phantom manipulator. For the remaining tasks, feedback is enabled and forces are calculated as a function of the 2D distance between the fixation point and the tool tip. Each profile implements a different force function. For example, profiles 3 and 4 are based on a linear spring, while profile 6 implements a logarithmic function.

For the second part of the 2D *GC motor channelling* study, the optimal manipulation profile identified in the previous experiment is adopted. This profile is then used to assess *GC motor channelling* over a number of force graduations (spring constant graduations). The same video, setup and task are used as with the first experiment with the same seven subjects. Initially, *GC motor channelling*

**Table 1**

The force and hand-motion scaling profiles (manipulation profiles) in the order as they are introduced during the 2D experiment. Both the X and Y axes represent the absolute distance between the fixation point and the tool-tip position on the image frame (i.e. pixels). The vertical axis (force) represents the normalized magnitude of the attractive force toward the fixation point exerted on the hand by the haptic device. Parameter  $k$  is the spring constant. In the table only the 1D and 2D cases are demonstrated, however, the same principles apply for the 3D case.

Profile	1D case	2D case	Description	Profile	1D case	2D case	Description
1			<ul style="list-style-type: none"> <li>No force exerted <math>F = 0</math>, GCMC off</li> <li>Hand-motion scaling: Profile 1: <i>High</i> Profile 2: (1:1)</li> </ul>	6			<ul style="list-style-type: none"> <li>Logarithmic force profile <math>F = k \cdot \log( x  + 1)</math></li> <li>Hand-motion scaling: (1:1)</li> </ul>
2			<ul style="list-style-type: none"> <li>Linear spring force <math>F = k \cdot x</math></li> <li>Hand-motion scaling: Profile 3: <i>High</i> Profile 4: (1:1)</li> </ul>	7			<ul style="list-style-type: none"> <li>Linear spring and constant force well <math>F = k \cdot x</math> for <math>-t &gt; x &gt; t</math>, else <math>F = const</math></li> <li>Hand-motion scaling: (1:1)</li> </ul>
3			<ul style="list-style-type: none"> <li>Exponential force profile <math>F = k \cdot (e^{ x } - 1)</math></li> <li>Hand-motion scaling: (1:1)</li> </ul>	8			<ul style="list-style-type: none"> <li>Linear spring and zero-force well <math>F = k \cdot x</math> for <math>-t &gt; x &gt; t</math>, else <math>F = 0</math></li> <li>Hand-motion scaling: (1:1)</li> </ul>
4							
5							

is enabled using a high spring constant. Gradually, the spring stiffness is reduced down to zero. To minimise the learning effect, the video was paused after five tissue deformation cycles over each manipulation profile and the subjects were asked to look away from the screen and leave hold of the haptic manipulator. After 20 s, the subjects were cued with a timed audible signal that the experiment is about to resume. Another 10 s were available for them to grasp the haptic manipulator and start fixating on the target to be tracked.

It should be noted that for both experiments manipulation was limited in 2D by constraining the haptic manipulation on a planar surface. This surface is defined by the  $X$  and  $Y$  axes on the manipulator frame-of-reference  $\mathbf{H}$  (Fig. 3). The orientation of the manipulation plane was set parallel to the screen during the initial calibration of the manipulator and remained the same for all subjects for the duration of the experiments. For both experiments, time, fixation, target and tool-tip coordinates were recorded for post processing. Analysis was based on measuring the error of the tool-tip position and the actual position of the tracked target.

In the following sections we will extend the current *GC motor channelling* framework for 3D manipulations and demonstrate how it can be used to implement *Gaze-Contingent Haptic Constraints (GC haptic constraints)*.

### 2.3. Principle of GC haptic constraints

For 3D experiments to be described below, a 3D heart model was reconstructed from MR images of a silicon phantom (Chamberlain Group, MA). Surface texture was also acquired and rendered to provide realistic visualisation (Fig. 4). The model was deformed between prescribed key frames. For this study, the principal modes of deformation were limited to the short and long axes of the heart. The two modes of deformation were harmonically combined to represent realistic cardiac motion.

For implementing *GC haptic constraints* in 3D, a binocular eye tracker was developed and integrated into the da Vinci surgical console (Fig. 4b). The eye tracker allows for seamless localization of the surgeon's 3D fixation point in relation to the operating

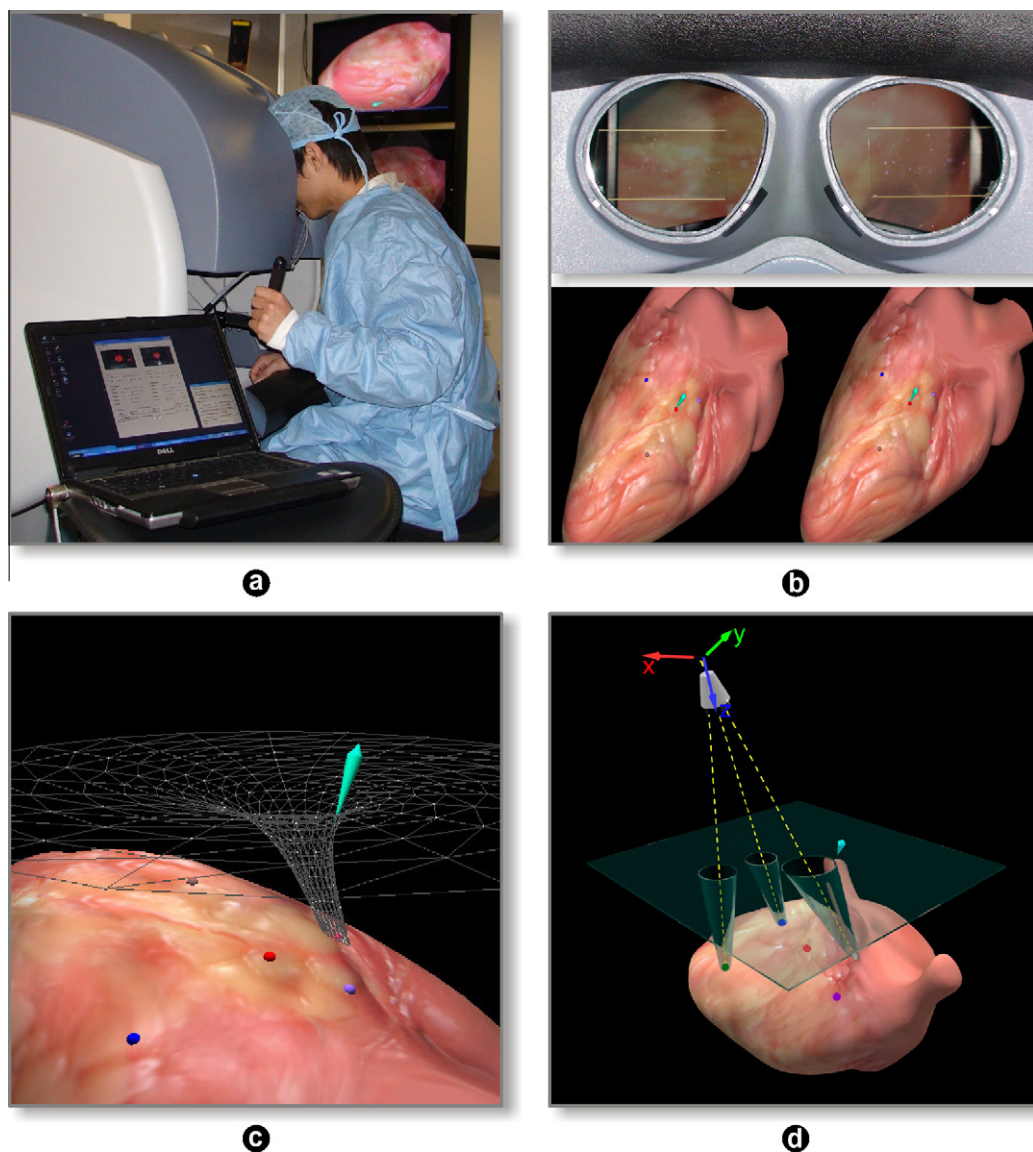


**Fig. 4.** In (a) the setup used with the *GC haptic constraints* experiments. A binocular eye tracker is integrated into the da Vinci stereoscopic console allowing tracking of the user's 3D fixation point while observing an artificially generated deforming heart (b). Five fiducial markers are locked onto the epicardium that are only accessible by manipulating the virtual tool through deformable conical pathways (c). In (d) a planar hard safety boundary is also introduced at a small distance from the cardiac surface.

FOV without obstructing the surgeon's direct vision. The device consists of a pair of near infrared sensitive cameras, an array of externally switchable sub-miniature IR emitting diodes at 940 nm and a pair of dichroic beam splitters with their cut-off wavelength set above 750 nm. This configuration provides appropriate illumination of the surgeon's eyes as their images are captured at a rate of 50 fps. The outputs from the two cameras are then digitized at a resolution of  $768 \times 576$  and processed in real-time. By calculating the corresponding ocular vergence, the 3D depth of the fixation point can be determined. The details of this implementation are described in detail in (Mylonas et al., 2004, 2006).

The haptic interaction within the simulated 3D surgical scene was applied based on the Euclidean distance between the 3D fixation point and the position of the manipulated surgical instrument as explained earlier and further illustrated in Fig. 3. Similarly to the 2D case, the generated force direction is towards the fixation point.

#### 2.4. Experimental setup for GC haptic constraints

To examine how the proposed *GC haptic constraints* concept can be used to provide haptic constraints in robot-assisted MIS procedures, six subjects were asked to observe the deforming 3D synthetic cardiac scene through the da Vinci stereoscopic console (Fig. 4a and b). Prior to each trial, all subjects underwent user specific binocular calibration. During the experiment, eye tracking provides the 3D fixation point. When *GC motor channelling* is enabled, the user feels forces in 3 DoF exerted to the virtual instrument according to the distance from the fixation point and the linear spring profile as this was presented in previous sections. In this case, the exerted force is proportional to the distance within a small preset range. Outside this range, the force magnitude is maintained constant. As before, all subjects were given time to be familiarised with the experimental setup. The task was to approach a preset fiducial with the virtual instrument and ablate it by pressing the manipulator button. Virtual ablation was performed only if the tool is within a radius of approximately 3 mm from the target when the button is pressed. A total of five fiducial markers locked onto the cardiac surface were displayed twice in a random order resulting in a total of 10 targets being introduced during the experiment. All subjects were presented with identical sequences. Throughout the study, time, instrument trajectory, target coordinates, fixations and relative position of the tool tip to the epicardium were recorded. Positive values indicate that the tool is safely in front of the visible part of the epicardium, while negative values indicate that the tool has penetrated into the heart muscle. The experiments were repeated twice, once with *GC haptic constraints* disabled and once more with *GC haptic constraints* enabled with these two selected in random order. When *GC haptic constraints* is enabled, a planar safety boundary is also introduced to prevent the instrument from crashing onto the tissue and cause inadvertent damage. The boundary is parallel to the  $x$ - $y$  plane of the virtual camera and its position on the  $z$  axis (depth) is determined by the depth of the first few fixations that were closer to the camera origin minus a small shift towards the origin (Fig. 4d). The only way for the virtual instrument to cross behind the hard safety boundary and touch the tissue is through narrow conical channels that are generated based on the position of each fiducial (Fig. 4c and d). The apex of a cone is inserted under the tissue surface slightly so that the virtual instrument is relatively free to move, track and ablate the deforming tissue. In this experiment, the vector connecting the apex and the base centre coincided with the vector connecting the camera origin and the fiducial. Only one cone was enabled at a time and this selection was based on the user's fixation point and a preset threshold.

### 3. Results

#### 3.1. Experimental results for GC motor channelling

For assessing the effectiveness of the proposed *GC motor channelling* concept, target, tool-tip and fixation point data was recorded throughout the eight manipulation profiles. The effectiveness of the scheme was judged according to its ability to reduce the motor tracking error of the deforming target. Error analysis was performed across all eight tested manipulation profiles and for all subjects.

The bar chart in Fig. 5 shows the mean motor tracking error for the eight manipulation profiles tested according to Table 1. It is evident that the error is reduced dramatically when *GC motor channelling* is enabled (columns 3–8). When a high hand-motion scaling factor is used (columns 1 and 3), the improvement is over 40%. Columns 2 and 4 show the free and *GC motor channelling* errors respectively for the 1:1 hand-motion scaling. The improvement in accuracy in this case is over 53%. From the same graph, it can also be observed that the optimal force profile is the linear spring model as shown in column 4. Apart from the reduced motor tracking error, it can be seen that this profile provides the best smoothness and haptic consistency. Along with the bar chart in Fig. 5, area plots of the motor tracking error across all subjects are generated. Areas in blue correspond to the free manipulation error for profile 2, while red areas are for the *GC motor channelling* enabled profile 4. The first column is the error on the  $X$  axis, the middle on the  $Y$  axis, while the column on the right is the Euclidian distance error. In all cases and for all subjects, initial inspection reveals the superiority of the *GC motor channelling*-enabled manipulation in reducing motor tracking error in both the  $X$  and  $Y$  directions.

Fig. 6 provides a side-by-side comparison of all subjects recorded data for manipulation profile 2 (left column) and profile 4 (right column). Each plot shows the fixation (green lines) and the tool-tip  $X$  and  $Y$  coordinates (blue lines) plotted along with the corresponding target trajectory (red lines). There are a number of useful observations we can make based on these plots. Firstly, it is apparent that *GC motor channelling* promotes motor tracking of the deforming tissue as the blue lines on the corresponding plots are more closely following the red lines. Another observation to make is that at times the fixations are offset from the target trajectory, especially in the  $Y$  axis. This can happen sporadically (e.g. subject 5) or for the whole duration of the task (e.g. subjects 1, 3, 4). The main reason for a consistent fixation path offset can be attributed to problems with eye tracking, largely due to inaccurate eye calibration. The plots in Fig. 6 reveal that although there is a considerable fixation offset from the target, the tool trajectory does not seem to be affected and even in these cases, it is closely following the target trajectory. It is hypothesised that with *GC motor channelling*, the fixation point can provide a stable trajectory reference. This behaviour seems to be congruent with the main characteristic of VFs. Another observation from the experiment is that the hand does not seem to be overpowered by the fixation point. From the same figure it is also inconclusive whether with *GC motor channelling* the eye precedes the hand. Previous research has shown that this can be influenced by a number of factors including the proficiency of manual control and the nature of tasks involved (Leong, 2009). From this figure, the results do not uniformly show whether with *GC motor channelling* the eye precedes the hand. In most cases, the fixation and hand motion data are synchronous (subjects 2, 4, 5, 7) but in the remaining cases the eye is at times slightly lagging behind the hand motion. It should be noted that the median filtering used actually introduced a temporal delay of 140 ms, so for subjects 2, 3, 5 and 7, the eye is leading the hand motion.



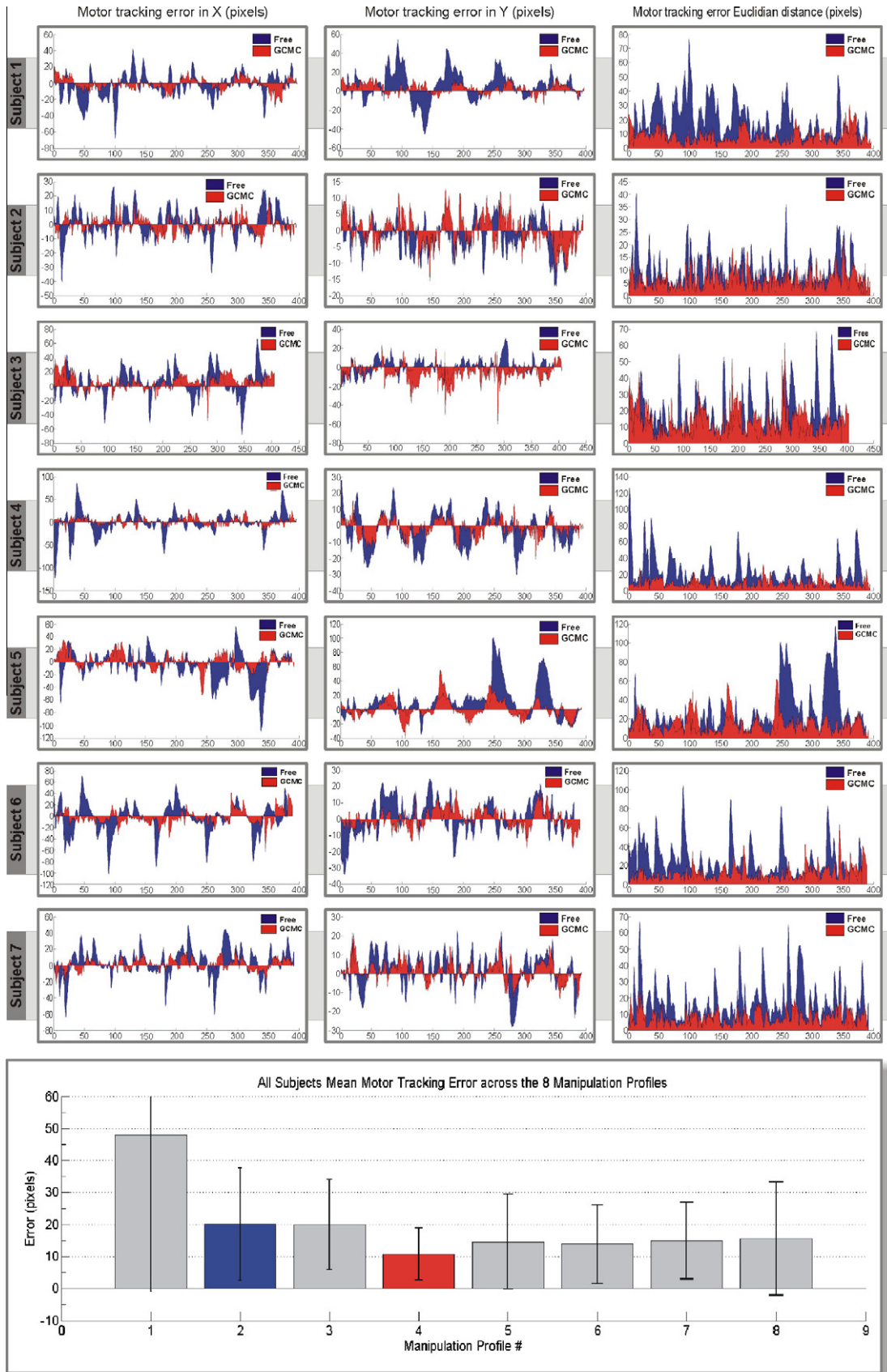
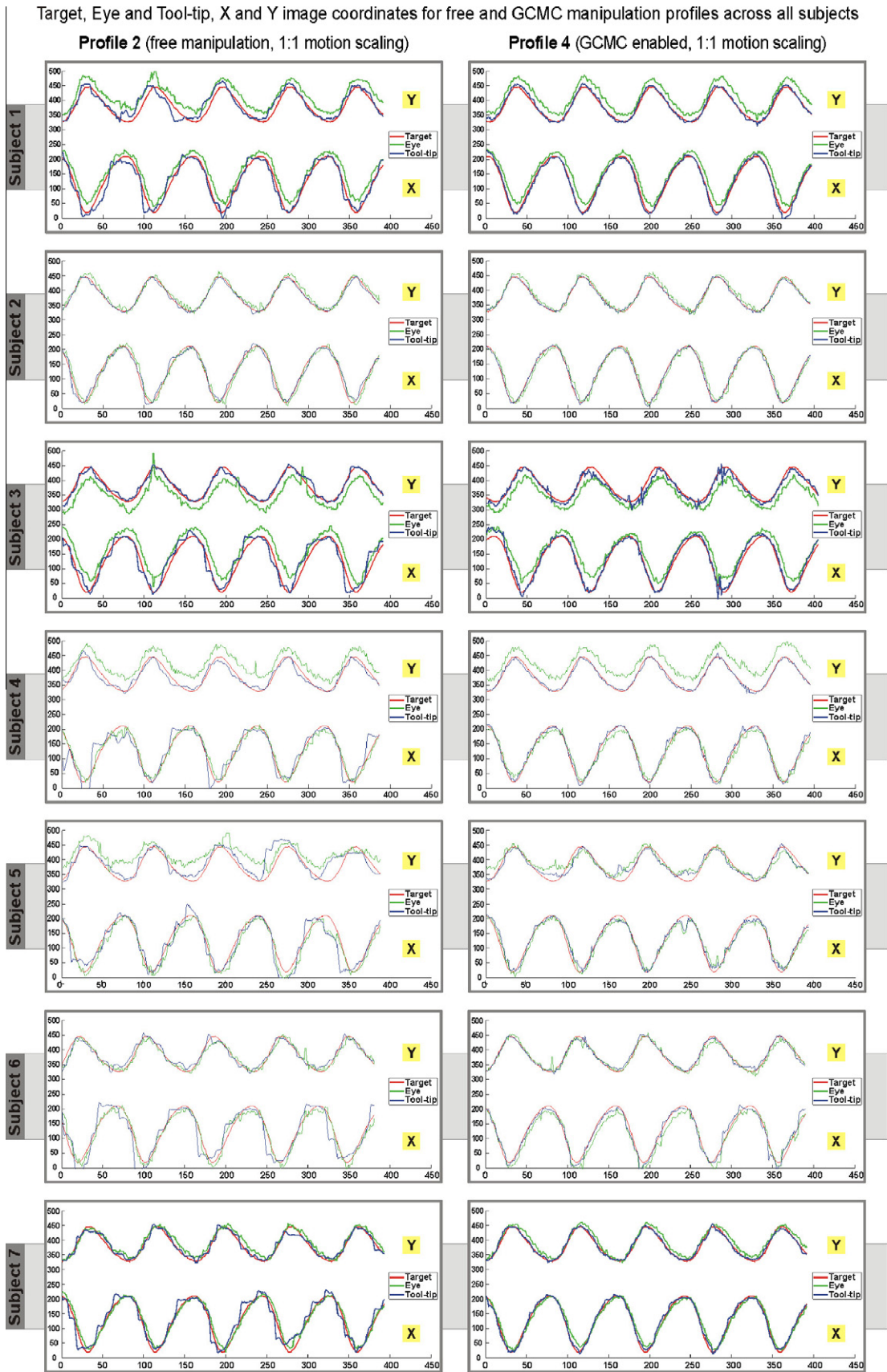
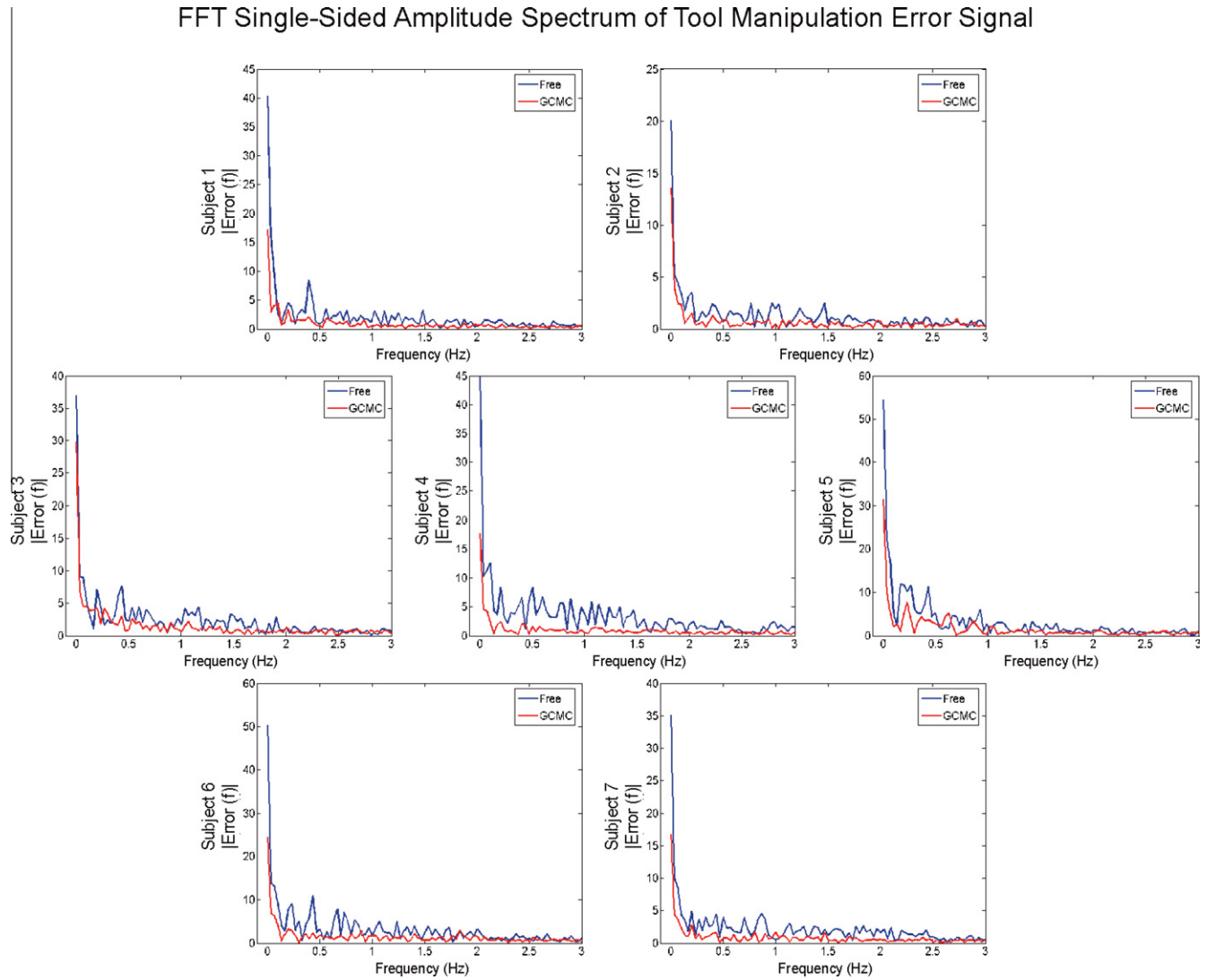


Fig. 5. Projected motor tracking error along the X (left), Y (middle) axes for all the subjects studied and the corresponding Euclidian distances (right column). The areas in blue correspond to the free manipulation profile 2 while the ones in red are for the GC motor channelling enabled profile 4. The bottom graph summarizes the mean error across all manipulation profiles. The bars correspond to different force profiles according to Table. The error bars show the standard deviation.



**Fig. 6.** Fixation and tool-tip X and Y coordinates plotted along with the corresponding target trajectory for all subjects. The column on the left corresponds to manipulation profile 2 (free, 1:1 motion scaling) while the column on the right is for profile 4 (*GC motor channelling* enabled, 1:1 motion scaling).



**Fig. 7.** Discrete Fourier Transform frequency analysis for all subjects of the free manipulation profile 2 and the *GC motor channelling* enabled profile 4. The power spectrum of the free manipulation profile (blue lines) exhibits more peaky behaviour from the *GC motor channelling* one (red lines). This signifies that *GC motor channelling* achieves smoother and less erroneous motor tracking of the moving target. (For interpretation of the references to colour in this figure legend, the reader is referred to the web version of this article.)

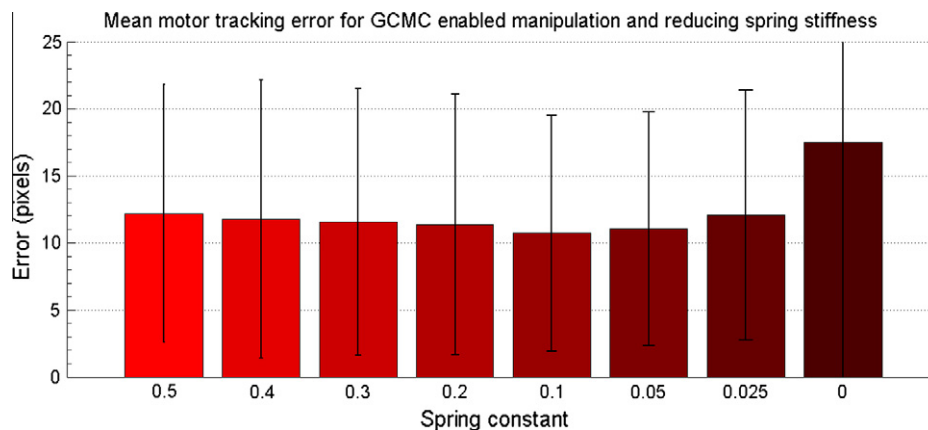


**Fig. 8.** The effect of spring stiffness on the accuracy of targeting when force profile 4 in (a) is adopted. Force decreases from left to right and the last column is the resulting error with forces disabled (i.e., free motion without any haptic constraints).

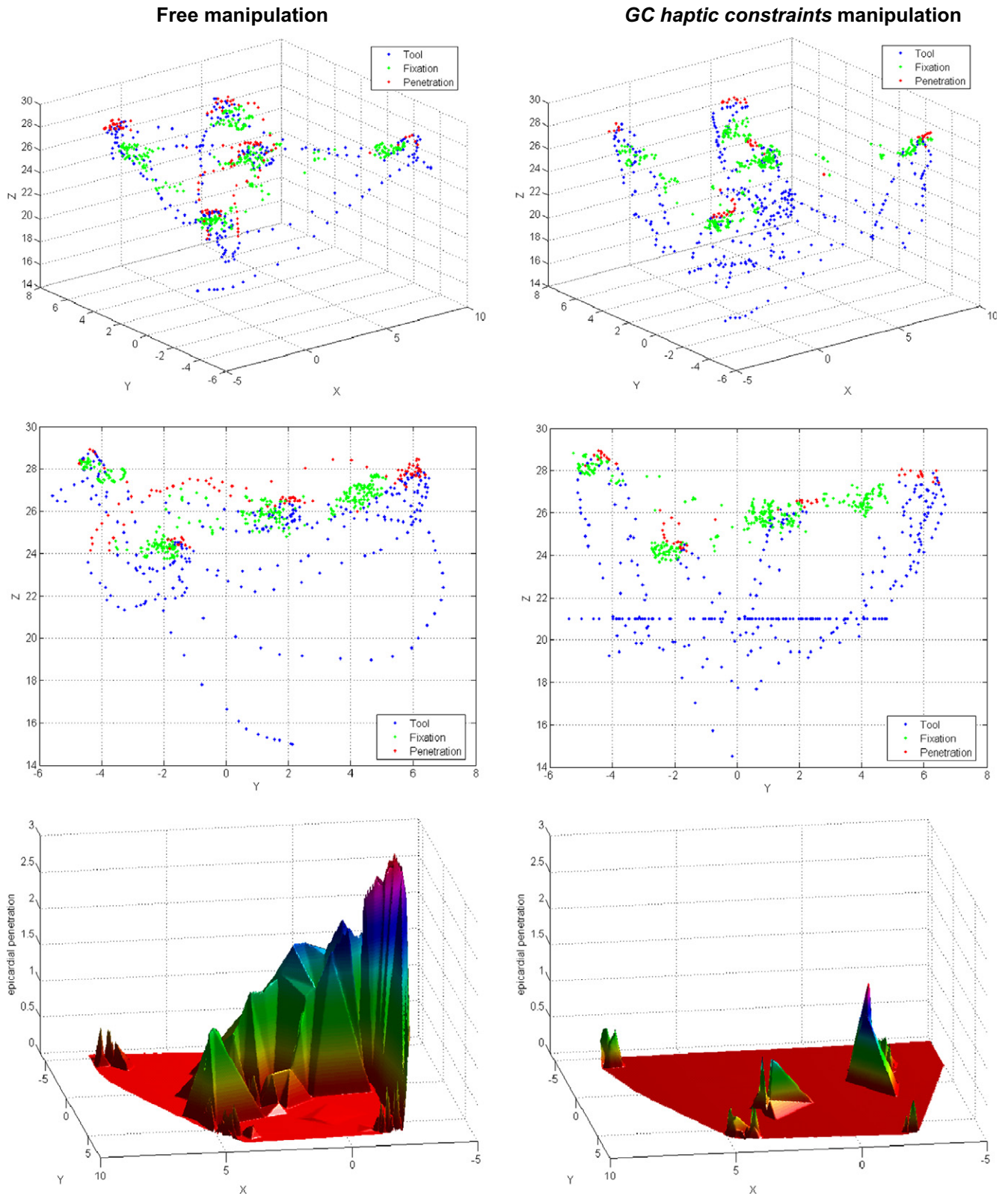


**Fig. 9.** Side-by-side comparison of the free and *GC haptic constraints* enabled manipulation for one of the subjects. The *top row* compares the 3D tool and fixation point trajectories. The red dots indicate the tool trajectory when epicardial penetration has occurred. The plots in the *middle row* are a 2D view of the same plots as above. For the *GC haptic constraints* case on the right, the linear clustering of tool trajectory points indicates where the planar safety boundary is placed. The *bottom row* of surface plots shows the amount of epicardial surface penetration (spatial occurrence and amplitude) during the two approaches. For the *GC haptic constraints* case the amount of penetration is clearly minimized.

To further support the above finding that *GC motor channelling* provides for smoother manipulation, Fourier analysis is performed on the tool manipulation signal. Fig. 7 shows the Fourier frequency

analysis of the free manipulation profile 2 and the *GC motor channelling* enabled profile 4 for all subjects. It is obvious that the power spectrum of the free manipulation profile (blue lines) has more

**Table 2**  
Results of the 3D experiments, comparing the amount of estimated tissue penetration and the accuracy of manually targeting the ablation targets with and without the use of GC haptic constraints. The results are averaged over all the participating subjects.

Method	Tissue penetration statistics averaged across all subjects						
	Number of times	Total duration (s)	Max duration (s)	Average duration (s)	Total length (mm)	Max length (mm)	Average length (mm)
Free average	17.17	33.25	4.52	1.62	233.14	48.04	12.69
Free std.	7.70	37.95	3.55	1.04	231.02	38.45	6.37
GC haptic constraints average	13.33	16.47	2.59	1.15	101.29	23.92	7.05
GC haptic constraints std.	6.77	10.04	1.12	0.24	96.34	17.71	3.80
% Improvement	22.33	50.46	42.55	29.08	56.55	50.22	44.47

high frequency jitter than that of the GC motor channelling (red lines). This supports the observation that GC motor channelling achieves smoother and less erroneous motor tracking of moving targets.

For the second part of the GC motor channelling study, the optimal manipulation profile 4 (linear spring force, 1:1 hand-motion scaling) was assessed over a number of spring constant graduations ( $k$ ). Fig. 8 shows the error analysis of the linear spring force model with different spring constants. Moving from left to right, the first column represents a stiffer spring exerting the highest force tested while the last column represents a spring with zero stiffness. It should be noted that the first column with a stiffness of 0.5 corresponds to a profile identical to the one responsible for the best performance on the first experiment (i.e., profile 4 in Fig. 5). Column 7 has a very low spring constant ( $k$ ) that is barely noticeable through the haptic device but still remains effective for reducing the error compared to the free manipulation task. From the same Fig. 8, we can also conclude that appropriate selection of a spring constant can result in further reduction of the manipulations error. For the experiments conducted, a spring constant of  $k=0.1$  introduces a smaller error compared to  $k=0.5$ , which is the one used for the first part of the GC motor channelling study. An optimal framework for parameter selection requires further investigation and it needs to take into account both the nature of the surgical task and the scaling factor used for hand motion.

### 3.2. Experimental results for GC haptic constraints

For the 3D GC haptic constraints experiments conducted, we have compared the amount of tissue penetration with and without the use of GC motor channelling. Tissue penetration occurs every time the virtual tool penetrates the surface of the tissue. Fig. 9 shows a side-by-side comparison of the free and GC haptic constraints enabled tasks for one subject. The column on the left corresponds to free manipulation, while the column on the right shows the results for the GC haptic constraints enabled task. The two plots on the top row compare the 3D tool and fixation point trajectories. The points in blue represent the tool trajectory, which are turned into red every time the surface is penetrated. The green points show the 3D fixation points. On the same plots, the five areas exhibiting the majority of points clustering correspond to the position of the five ablation targets that have been fixated and ablated at twice.

In the middle row of Fig. 9, the trajectories are projected onto the Y–Z plane. This helps to illustrate how much GC haptic constraints has helped to reduce the amount of penetration into the myocardium. This is indicated by the significantly reduced occurrence of tool trajectory points for the GC haptic constraints case. The same plot also clearly shows the presence and the advantage of the hard planar safety boundary introduced during the experiments. The position of the boundary is revealed by the planar clustering (appearing linear in 2D) of the tool trajectory points at about

21 mm along the Z axis. By comparing the two plots, it is evident that the safety boundary allowed elimination of those transitional tool trajectories that accidentally travel through the epicardial surface. Instead, manipulation in between the targets is achieved through the conical channels and the area behind the safety boundary.

The two surface plots in the bottom row of Fig. 9 compare the amount of epicardial surface penetration (spatial occurrence and amplitude) during the two tasks. For the GC haptic constraints case, the amount of penetration is clearly minimized as the majority of the surface appears as a plateau with only minor spikes of low frequency and small amplitude. Table 2 demonstrates the overall results for the six subjects studied. It is evident that there is a clear reduction in terms of the amount of penetration when GC haptic constraints is enabled with an improvement of 22.33% on the number of times the surgical tool has penetrated the tissue and 29.08% on the average penetration duration. Furthermore, the accuracy of manually targeting the ablation target has improved by 37.72%.

### 4. Assessment of GC motor channelling-induced cognitive demand with fNIRS

In the previous sections, we have demonstrated how to create an additional sensorimotor pathway which directly connects the visual and motor channels. Through the use of GC motor channelling, we have demonstrated improved hand–eye coordination and target tracking. One potential question to be asked is whether the “blasphemy” of interfering with the natural flow of sensorimotor information has any underlying effects on the human mental processes. Most importantly, the associated cognitive load, if any, has to be measured. In order to answer these questions, we need to gain insight into the human brain’s cognitive processes. fNIRS is a relatively recent technique that could potentially expose the underlying cognitive demand involved in GC motor channelling. fNIRS is a non-invasive optical neuroimaging modality capable of detecting changes in brain haemodynamics which are reflective of the brain’s function through “neurovascular coupling” (Maki et al., 1995; Hoshi, 2007). The term “neurovascular coupling” describes the way in which cerebral blood flow (CBF) is coupled to the cerebral metabolic rate of oxygen (CMRO<sub>2</sub>). It has been widely accepted that within a short period after the onset of localized brain activity induced by somatosensory stimulation, there is an increase of CBF, which is larger than the concomitant increase in oxygen consumption (Fox and Raichle, 1986). This results in a local increase in the concentration levels of oxy-haemoglobin (HbO<sub>2</sub>) and a drop in deoxy-haemoglobin (HHb) in activated brain regions. With fNIRS, it is possible to measure relative changes in the concentrations of HbO<sub>2</sub>, HHb as well as their sum total haemoglobin (HbT). For more detailed discussions about the principles of fNIRS the reader is referred to a number of publications elsewhere (Villringer and Chance, 1997; Strangman et al., 2002; Hoshi, 2007; Leff, 2009).

Evidence from the motor learning literature emphasizes the importance of the prefrontal cortex (PFC) in the acquisition of skilled task performance (Kelly and Garavan, 2005; Halsband and Lange, 2006). There is a tendency for learners to activate the PFC when demands are novel and performance is erratic and highly piecemeal (Shadmehr and Holcomb, 1997; Sakatani et al., 1999, 2003; Tracey and Lathan, 2001; Debaere et al., 2004; Leff et al., 2008, 2009). In contrast, automated expert performance is associated with PFC redundancy (Jenkins et al., 1994; Puttemans et al., 2005). It is anticipated that during a complex monoscopic visuomotor target localization task, PFC activation will reflect the novice's attention and concentration until the deformation sequence/motion trajectory are internalised. It is hypothesized that GC motor channelling-assistance will improve the technical precision of the operator by alleviating the cognitive burden of the task.

#### 4.1. fNIRS assessment of PFC response

To assess the cognitive demand associated with the use of GC motor channelling, identical methods as in the corresponding study described previously have been used. The experiments involved free and GC motor channelling-enabled control and concomitant measuring of the corresponding PFC activation.

For monitoring brain haemodynamics, fNIRS is performed with a continuous-wave Hitachi ETG-4000 (Hitachi Ltd.) optical topog-

raphy system. For this study, cortical activity is assessed from 24 scalp positions arranged in two  $3 \times 3$  source-detection configurations, similar to the ones shown in Fig. 10d, covering a total area of  $6 \text{ cm} \times 6 \text{ cm} = 36 \text{ cm}^2$ . The optode arrays are positioned over the prefrontal cortex according to the Unambiguously Illustrated 10/10 system (UI 10/10) (Jurcak et al., 2007). The left inferomedial and inferolateral optodes are positioned over Fp1 and F7 respectively and the right inferomedial and inferolateral optodes are positioned over Fp2 and F8. The light detected by each detecting probe is the mixture of multiple sources at wavelengths of 695 nm and 830 nm. Sampling is simultaneous and at 10 Hz. After conversion of light measurements to haemoglobin levels by spectroscopic and spatial reconstruction, haemodynamics can be displayed either as linear time course plots or as topographs as illustrated in Fig. 10c.

Twenty-one healthy subjects, 18 males and 3 females, with ages between 24 and 37 (mean 28.8) participated in this study. All subjects performed two tasks during the experiment; control (free manipulation) and GC motor channelling-enabled manipulation. The experimental setup was identical to the one presented in the GC motor channelling section earlier. The ordering of the tasks was randomized. Both tasks were presented following a block paradigm design. For each task, a 30 s baseline of optical data was first collected. Tasks were then repeated five times during blocks of 20 s with inter-trial rests of 30 s, and finalised with another 30 s rest. During the rest periods a black screen substituted the video

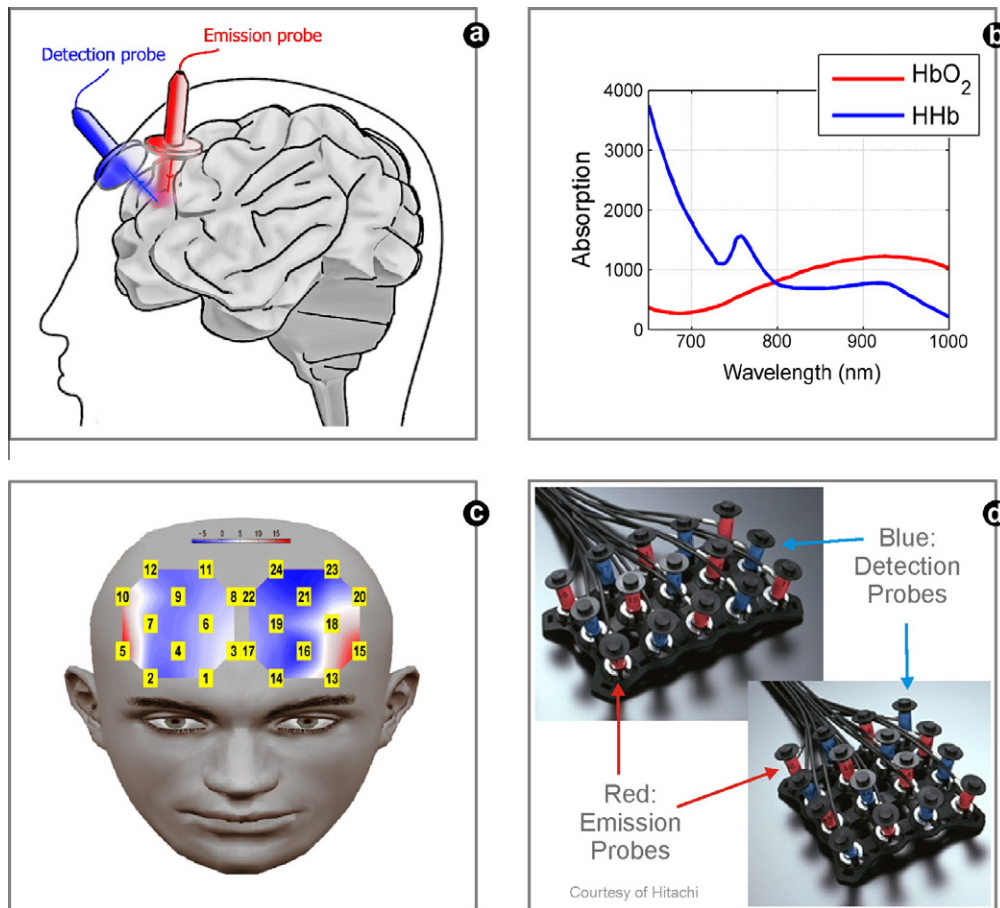


**Fig. 10.** (a) In fNIRS, emission probes are used to shine near-infrared light through the scalp. Here, the light distribution as it travels from the source to the detector is shown. Along its path-length the photons must travel through the scalp, skull, meninges, and finally reach the cortex before being backscattered to the detection probe. (b) The graph shows the different absorption characteristics of oxy- and deoxy-haemoglobin as their absorption spectra are crossing at the isosbestic point  $\sim 800 \text{ nm}$  (adapted from Leff (2009)). (c) Multiple light reflectance measures are combined to provide functional maps known as optical topographs. (d) Multiple emitter and detector arrays are used in modern NIRS devices with  $3 \times 3$ ,  $3 \times 5$  or  $4 \times 4$  configurations possible.

stream. Switching from task to rest was automatically indicated with a beeping cue. A schematic of the experimental protocol is illustrated in Fig. 11.

Participants were given the opportunity to familiarise with the *GC motor channelling* paradigm by means of an ad hoc shooting game. The goal of the game is shooting at flying targets appearing on the computer screen. The game involves three different stages each one lasting 2 min. For the first stage, the subjects aim at the targets using free manipulation with any forces disabled. The haptic phantom is simply used as a joystick to control the position of the aiming crosshair on the screen and the button on its handle is used as the trigger. For the second stage, the subjects aim at the targets purely using their gaze. Finally, the last 2 min of the training involve the full usage of the *GC motor channelling* paradigm where the subjects control the position of the aiming crosshair using the manipulator, while forces are exerted according to the position of their fixation point on the screen. As it is the case for all *GC motor channelling* experiments, the hand is not overpowered by the haptic phantom so the users are free to perform small corrections with their hands on top of the fixation point. Pictures of the set up and a snapshot of the training game are shown in Fig. 12.

After training, the participants are carefully measured for *fNIRS* optode placement and a number of landmarks are marked. The optode arrays are then positioned based on specific markers and standard positions according to the UI 10/10 system (Jurcak et al., 2007). The arrays are secured with two foam and Velcro bandages, ensuring no subject discomfort whilst minimising movement artefact, and are covered with a black cloth to eliminate light interference.

Prior to performing the tasks, the volunteers were shown and tried each experimental task once, with and without feedback. Then, both tasks were sequentially executed following the block design paradigm that was described earlier and is schematically illustrated in Fig. 11.

#### 4.2. *GC motor channelling* and *fNIRS* results

The task performance results for all subjects did not show any differences to what it was expected, i.e., the subjects managed to keep the tool tip closer to the target, and their hand movements

were smoother. Similarly to the results presented in earlier sections, the motor tracking error was significantly reduced for the *GC motor channelling*-enabled task compared to the free manipulation task. The results for the cortical activity associated with each of the two tasks, were however not expected.

##### 4.2.1. Cortical activity

Fig. 13a illustrates the results from exemplary subject 14. It shows the haemodynamic behaviour captured by optode Channel 1 averaged across the five trials for both experimental tasks. The graph on the left corresponds to the free manipulation task which did not trigger any consistent task related changes in cortical haemodynamics. The graph on the right, corresponds to the *GC motor channelling*-enabled task, clearly demonstrating the pattern which is typically associated with cortical activity. The need to supply oxygen to activated brain regions accounts for the rapid rise in  $\text{HbO}_2$ . Due to the increase in cerebral blood flow, HHb is washed out of an area faster than it can be produced by the deoxygenation of  $\text{HbO}_2$ . This translates to an increase in  $\text{HbO}_2$  (indicated by the red line) and a decrease in HHb (indicated by the blue line) a few seconds after the stimulus.

A topographical reconstruction of the mean activity for one of the subjects (subject 12) during both tasks is illustrated in Fig. 13b. The plot on the left corresponds to the control task (i.e. free manipulation), while the column on the right correspond to the stimulus task (i.e. *GC motor channelling*-enabled manipulation). The values at the channels were calculated by subtracting the mean value during the task period minus the mean value of 5 s worth of baseline. Topological reconstruction was performed by linear interpolation. Striking differences in the haemodynamic patterns between the two tasks can be appreciated, with the *GC motor channelling* task being more cognitively demanding. This is especially evident in the  $\text{HbDiff} = \text{HbO}_2 - \text{HHb}$  topographs shown here exposing oxygen saturation.

For all the subjects studied, cortical activity for the available channels is established by the *Wilcoxon* sign rank test. This is illustrated in Fig. 13c for both the control and the stimulus tasks. Channels 1, 4, 6, 7, 9, 16, 19 and 21, mostly in the central PFC, correspond to those channels exhibiting increase in  $\text{HbO}_2$  accompanied with a decrease in HHb (i.e. the typical pattern correspond-

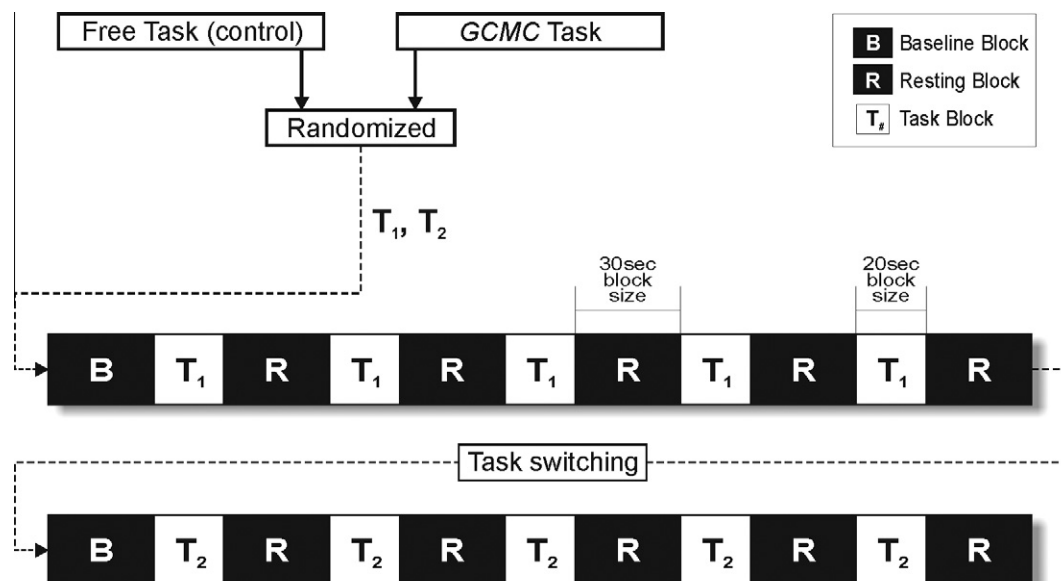


Fig. 11. Block diagram of the two performed tasks (free and *GC motor channelling*) for the *fNIRS* experiment. Task blocks ( $T_*$ ) with duration of 20 s are used, interrupted by 30 s long resting blocks (R). A 30 s baseline data collection block (B) is allocated at the beginning of each task. The order of the two tasks is randomized prior to data collection.





Free manipulation (Control Task)

GCMC enabled manipulation (Stimulus Task)

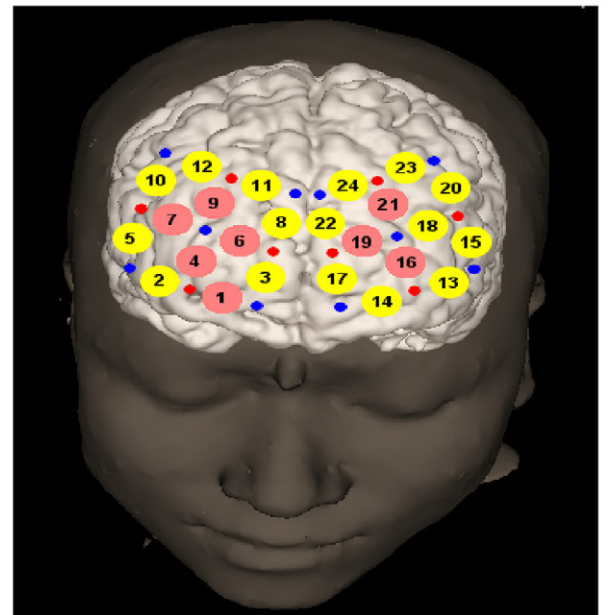
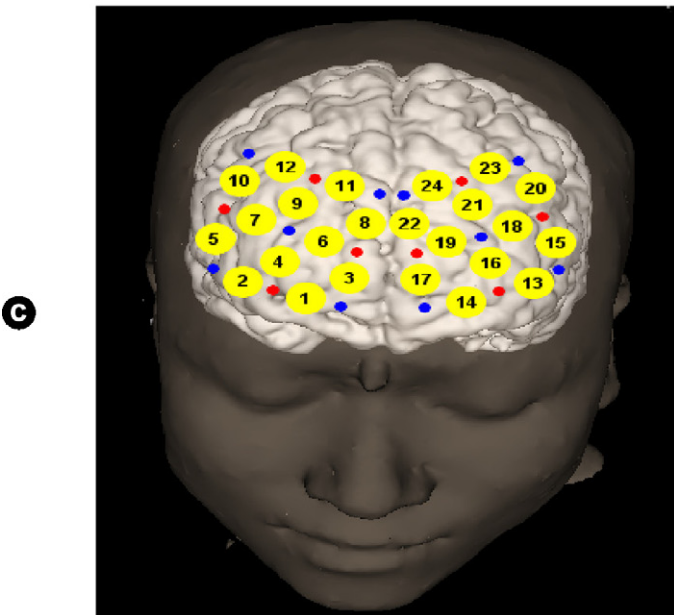
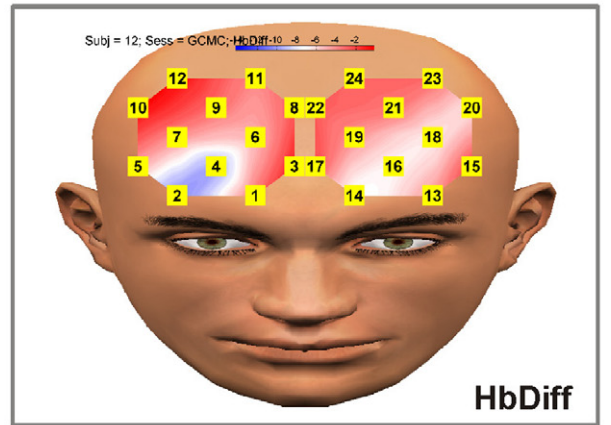
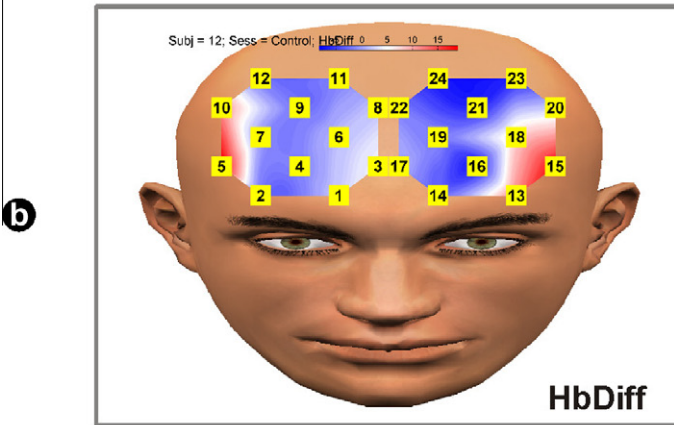
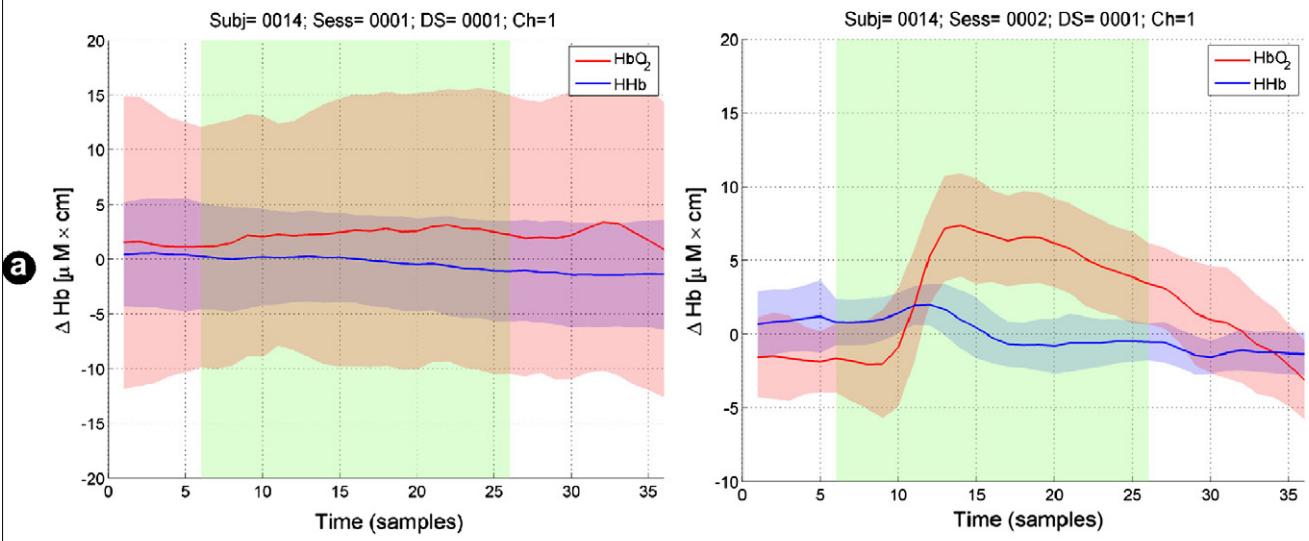


**Fig. 13.** In all cases, the left column corresponds to free manipulation while the right one to GC motor channelling-enabled manipulation. (a) Haemodynamic behaviour captured by optode Channel 1 averaged across the five trials for subject 14. For free manipulation, no activation is observed. For the *GC motor channelling* case, the typical activation pattern of brain haemodynamic response is clearly visible. It is indicated by a rise in the oxy-haemoglobin (red line) signal 2 or 3 s after the task onset, accompanied by a decreased in deoxy-haemoglobin (blue line). The associated red and blue shaded regions indicate the standard deviation across the five trials. The green patch corresponds to the task time. Decimated at 1 Hz, the number of samples can be extrapolated to seconds. (b) HbDiff topographical representation of typical average changes in haemodynamics during the tasks for subject 12. Striking differences in the haemodynamic patterns between the two tasks can be appreciated, with the *GC motor channelling* tasks being more cognitive demanding. (c) Representation of the statistical analysis of activity across all subjects. Channels highlighted in pink correspond to those channels exhibiting increase in HbO<sub>2</sub> accompanied with a decrease in HHb, and where at least one of which reached statistical significance. (For interpretation of the references to colour in this figure legend, the reader is referred to the web version of this article.)

control of the surgical tool. This fact explains why possible inaccuracies in eye tracking can be compensated for through small hand adjustments from the users. Future work should concentrate on implementing deformable pathways and boundaries that will allow dynamic haptic constraints for more complex anatomical structures. Aspects of this work are already undergoing (Kwok et al., 2009).

In the current study, a linear spring model has been found to generate the best results in terms of haptic guidance. A number of different models are already available in the literature suggesting that a mass-spring-damper model may give better results. This has not been tested in this study and deserves further investigations. However, to some extent, a mass-spring-damper model is al-

ready implicitly implemented with the current study. The main reason is that the fixation signal is already median filtered. With the exerted forces relying upon the relative position of the fixation point and the manipulator, this effectively means that the causal effect of force exertion is already damped through the fixation filtering. An issue related to this is the need to clearly understand the effect of motion dampening during motor tracking of a moving target. This will help to understand to which degree improved motor tracking accuracy can be attributed to the use of the *Gaze-Contingent* framework alone and to which degree to the indirect motion dampening as discussed earlier. Further work should be conducted to decouple of these factors. Another interesting aspect would be to evaluate different force implementation strategies such us

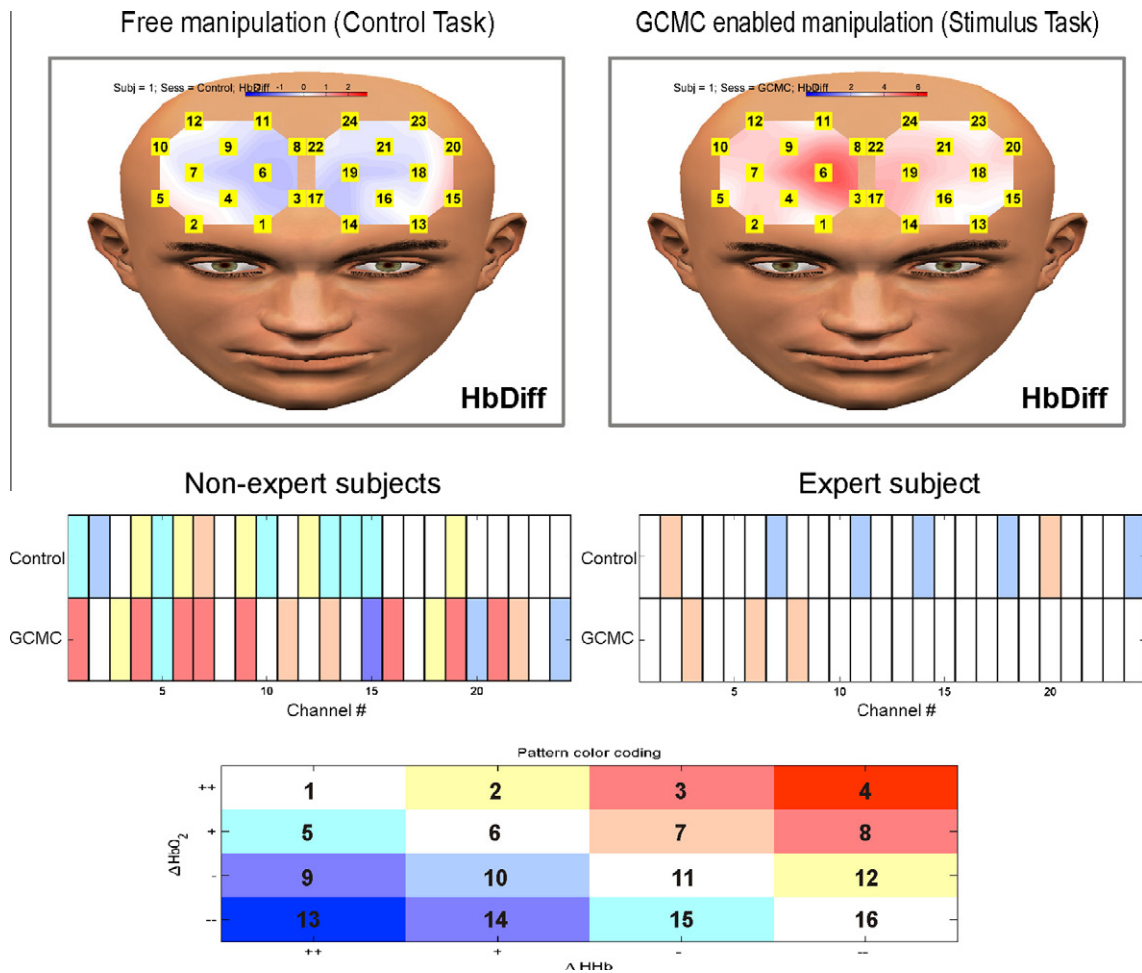


**Fig. 14.** On the top, the topographs showing the haemodynamic changes of the only expert subject in the *GC motor channelling* concept. Comparing the left and right topographs for HbDiff, it is easy to conclude that there are only minor differences between the two. Where some differences occur, these seem to manifest around a single channel (here channel 6). This signifies that there is no significant cognitive load associated with the performance of the *GC motor channelling*-enabled task. On the bottom, comparison of the activity matrices for the non-expert subjects (left) and the single expert subject (right). Colour pattern 4 is classic activation while pattern 13 is classic deactivation. It is apparent that for the expert subject, activation is very subtle and occurs on very few channels, while for the non-expert subjects activation borders the classic activation pattern 4.

repelling instead of attracting forces between the fixation point and the hand to avoid critical anatomical regions.

Another point that deserves further investigation is the effect of latency in the master–slave, the stimulus display, and the eye-tracking systems. That is the effect in terms of performance, transparency and stability on the proposed GCMC framework. Although this has not been studied in detail, it is expected that prediction models based on fixation trajectory and saccadic dynamics could help in dealing with these problems. For *in vivo* and general application of the proposed method, it will also be necessary to take into account subject specific behaviour of hand–eye coordination but also the fact that non-periodic motion tasks may be involved. In general surgical tasks, it might be necessary to supplement gaze information with 3D computer vision algorithms. We believe that the synergistic use of traditional computer vision techniques and perceptually enabled approaches (like the one presented in this paper) can maximize the benefits of the framework proposed.

A very interesting aspect that emerged through the course of this work is related to the cognitive load involved with the *GC motor channelling* concept. The experimental findings show striking differences in terms of the degree of brain activation between expert and non-expert subjects, with the expert exhibiting no cognitive load. Elucidating plausible explanations for this behaviour requires further investigations.

In the current study, the results seem to suggest that for complex tasks, the use of assistive guidance, i.e., *GC motor channelling* or *GC haptic constraints*, allows the user to focus more on the quality of task execution, particularly for novices. This is evident from the quality of the motion trajectories and improved accuracy of targeting. We have demonstrated in previous studies that for simple tasks such as surgical knot tying, reduced PFC engagement is observed when the task performance has reached fluency (Leff et al., 2008). We hypothesise therefore, with the introduction of *GC motor channelling* or *GC haptic constraints*, novices are able to rapidly attain basic competency in task performance and focus on task planning and the quality of manoeuvres, thus initially invoking an increased engagement of PFC. As the performance becomes more consistent and has reached fluency, a reduced PFC may be observed, reflecting a reduced cognitive burden. It is conceivable that for the complete novice, the initial trials are used to explore the challenges of the task to better direct attention and concentration, and hence the need for greater PFC recruitment in subsequent trials.

In this instance, *GC motor channelling* enables naïve learners to make better use of prefrontal resources, enhancing their attention and concentration which results in improved technical performance. *GC motor channelling*-assistance may shift the subject along the learning curve toward the novel-intermediate phase of task performance during which PFC activation is predictable. Current undergoing studies will also attempt to compare the degree of brain activation evoked between GCMC-assisted novice and intermediate/advanced unaided performance. For the presented experiments, all subjects – but one – were novices and completely naive to the task and there was not a longitudinal/repeated measures element to the task (except within one trial).

It is expected that these results have practical significance in performing and learning robotic procedures. Gaze contingent assistance appears to improve technical precision possibly by enhancing the operator's ability to engage their neuronal centres associated with attention, concentration, performance monitoring and spatial memory.

## Acknowledgements

The authors would like to acknowledge the financial support from the EPSRC and the Hamlyn Centre for Robotic Surgery.

## References

- Abbott, J., Marayong, P., et al., 2007. Haptic virtual fixtures for robot-assisted manipulation. *Robotics Research* 5, 49–64.
- Davies, B., 2006. Active Constraints for Robotic Knee Surgery. *Robotic Surgery: The Kindest Cut of All*, 2006. The Institution of Engineering and Technology Seminar on (Ref. No. 2006/11372).
- Davies, B., Jakopec, M., et al., 2006. Active-constraint robotics for surgery. *Proceedings of the IEEE* 94 (9), 1696–1704.
- Debaere, F., Wenderoth, N., et al., 2004. Changes in brain activation during the acquisition of a new bimanual coordination task. *Neuropsychologia* 42 (7), 855–867.
- Fox, P.T., Raichle, M.E., 1986. Focal physiological uncoupling of cerebral blood flow and oxidative metabolism during somatosensory stimulation in human subjects. *Proceedings of the National Academy of Sciences of the United States of America* 83 (4), 1140–1144.
- Halsband, U., Lange, R.K., 2006. Motor learning in man: a review of functional and clinical studies. *Journal of Physiology – Paris* 99 (4–6), 414–424.
- Hoshi, Y., 2007. Functional near-infrared spectroscopy: current status and future prospects. *Journal of Biomedical Optics* 12 (6), 062106.
- Jenkins, I.H., Brooks, D.J., et al., 1994. Motor sequence learning: a study with positron emission tomography. *Journal of Neuroscience* 14 (6), 3775–3790.
- Jurcak, V., Tsuzuki, D., et al., 2007. 10/20, 10/10 and 10/5 system revisited: their validity as a relative head-surface-based positioning systems. *NeuroImage* 34, 1600–1611.
- Kelly, A.M., Garavan, H., 2005. Human functional neuroimaging of brain changes associated with practice. *Cerebral Cortex* 15 (8), 1089–1102.
- Kwok, K.-W., Mylonas, G., et al., 2009. Dynamic active constraints for hyper-redundant flexible robots. In: *Medical Image Computing and Computer-Assisted Intervention – MICCAI 2009*, pp. 410–417.
- Leff, D.R., 2009. An Assessment of Cortical Function in Expert and Novice Surgeons. Royal Society/Wolfson Foundation Medical Image Computing Laboratory. PhD, Imperial College London, London, p. 298.
- Leff, D.R., Elwell, C.E., et al., 2008. Changes in prefrontal cortical behaviour depend upon familiarity on a bimanual co-ordination task: an fNIRS study. *NeuroImage* 39 (2), 805–813.
- Leff, D.R., Orihuela-Espina, F., et al., 2009. Circadian cortical compensation: a longitudinal fNIRS study of sleep deprivation in surgical trainees. *Annals of Surgery*, in press.
- Leong, J.H.J., 2009. Hand–Eye Coordination in Surgery. Department of Biosurgery and Surgical Technology Royal Society/Wolfson Foundation Medical Image Computing Laboratory Imperial College London University of London. PhD, Imperial College London, London, p. 219.
- Leong, J., Atallah, L., et al., 2008. Investigation of partial directed coherence for hand–eye coordination in laparoscopic training. *Medical Imaging and Augmented Reality*, 270–278.
- Li, M., Taylor, R.H., 2004. Spatial motion constraints in medical robot using virtual fixtures generated by anatomy. In: *Robotics and Automation, 2004. Proceedings. ICRA '04. 2004 IEEE International Conference on*.
- Maki, A., Yamashita, Y., et al., 1995. Spatial and temporal analysis of human motor activity using non-invasive NIR topography. *Medical Physics* 22 (12), 1997–2005.
- Mylonas, G.P., Darzi, A., et al., 2004. Gaze contingent depth recovery and motion stabilisation for minimally invasive robotic surgery. *Medical Imaging and Augmented Reality*, 311–319.
- Mylonas, G.P., Stoyanov, D., et al., 2005. Gaze-contingent soft tissue deformation tracking for minimally invasive robotic surgery. In: *Medical Image Computing and Computer-Assisted Intervention – MICCAI 2005*, pp. 843–850.
- Mylonas, G.P., Darzi, A., et al., 2006. Gaze-contingent control for minimally invasive robotic surgery. *Computer Aided Surgery* 11 (5), 256–266.
- Noonan, D.P., Mylonas, G.P., et al., 2008. Gaze contingent articulated robot control for robot assisted minimally invasive surgery. In: *Intelligent Robots and Systems, 2008. IROS 2008. IEEE/RSJ International Conference on*.
- Okamura, A.M., 2004. Methods for haptic feedback in teleoperated robot-assisted surgery. *Industrial Robot: An International Journal* 31 (6), 499–508.
- Park, S., Howe, R.D., et al., 2001. Virtual fixtures for robotic cardiac surgery. In: *Proceedings of the 4th International Conference on Medical Image Computing and Computer-Assisted Intervention. Springer-Verlag*.
- Puttemans, V., Wenderoth, N., et al., 2005. Changes in brain activation during the acquisition of a multifrequency bimanual coordination task: from the cognitive stage to advanced levels of automaticity. *Journal of Neuroscience* 25 (17), 4270–4278.
- Ren, J., Patel, R.V., et al., 2008. Dynamic 3-D virtual fixtures for minimally invasive beating heart procedures. *Medical Imaging, IEEE Transactions on* 27 (8), 1061–1070.
- Rosenberg, L.B., 1993. Virtual fixtures: perceptual tools for telerobotic manipulation. In: *Virtual Reality Annual International Symposium, 1993. IEEE*.
- Sailer, U., Flanagan, J.R., et al., 2005. Eye–hand coordination during learning of a novel visuomotor task. *Journal of Neuroscience* 25 (39), 8833–8842.
- Sakatani, K., Lichty, W., et al., 1999. Effects of aging on language-activated cerebral blood oxygenation changes of the left prefrontal cortex: near infrared spectroscopy study. *Journal of Stroke Cerebrovascular Diseases* 8 (6), 398–403.
- Sakatani, K., Murata, Y., et al., 2003. BOLD functional MRI may overlook activation areas in the damaged brain. *Acta Neurochirurgica* 87 (Suppl.), 59–62.

- Shadmehr, R., Holcomb, H.H., 1997. Neural correlates of motor memory consolidation. *Science* 277 (5327), 821–825.
- Strangman, G., Boas, D.A., et al., 2002. Non-invasive neuroimaging using near-infrared light. *Biological Psychiatry* 52, 679–693.
- Tobii-Technology, 2003. User Manual.
- Tracey, M.R., Lathan, C.E., 2001. The interaction of spatial ability and motor learning in the transfer of training from a simulator to a real task. *Studies in Health Technology and Informatics* 81, 521–527.
- Villringer, A., Chance, B., 1997. Non-invasive optical spectroscopy and imaging of human brain function. *Trends in Neuroscience* 20 (10), 435–442.
- Yang, G.-Z., Dempere-Marco, L., et al., 2002. Visual search: psychophysical models and practical applications. *Image and Vision Computing* 20 (4), 291–305.
- Yang, G.-Z., Mylonas, G., et al., 2008. Perceptual docking for robotic control. *Medical Imaging and Augmented Reality*, 21–30.